Deformation and Damage Mechanisms of Zinc Coatings on Hot-Dip Galvanized Steel Sheets: Part I. Deformation Modes

RODOLPHE PARISOT, SAMUEL FOREST, ANDRÉ PINEAU, FRANÇOIS GRILLON, XAVIER DEMONET, and JEAN-MICHEL MATAIGNE

Zinc-based coatings are widely used for protection against corrosion of steel-sheet products in the automotive industry. The objective of the present article is to investigate the deformation modes at work in three different microstructures of a thin (8 μm) zinc coating on an interstitial-free steel substrate under tension, plane-strain tension, and expansion loading. Damage mechanisms are addressed in a companion article. The plastic slip and twinning activity in the zinc grains of an untempered cold-rolled coating (labeled NSK), a tempered cold-rolled coating (labeled SK), and a recrystallized coating are compared with the response of the corresponding bulk low-alloyed zinc material. The in-plane grain size in the NSK and SK coatings ranges from 300 to 600 μm, *vs* about 30 μm in the recrystallized coating and bulk material. The coatings exhibit a strong crystallographic texture, with the *c*-axis generally normal to the sheet plane. Basal slip is shown to be the main deformation mechanism in bulk zinc and the recrystallized coating, whereas pyramidal π_2 slip and mechanical twinning are found to be major modes in the NSK and SK coatings. These results, obtained from an extensive, quantitative slip-line analysis combined with electron backscattered diffraction (EBSD) measurements, are explained by the constraining effect of the substrate. This effect is successfully modeled using a simple Taylor-like polycrystalline approach. The recrystallized coating behaves much like the bulk material. The interpretation of this grain-size effect between the NSK and SK coating, on the one hand, and the recrystallized coating, on the other hand, requires a full three-dimensional finite-element analysis of the multicrystalline coating provided in this work. The simulations show that strong strain gradients can develop in the recrystallized coating from the interface to the surface, which is not the case in the NSK and SK coatings.

I. INTRODUCTION

ZINC-based coatings are widely used for the protection against corrosion of steel-sheet products in the automotive industry.[1] A precise knowledge of their deformation and damage modes at work during stamping processes, for instance, is necessary to avoid the apparent degradation of the surface aspect and of the forming tools. Moreover, recent improvements in the metallurgy and material processing of such coatings have dramatically changed the properties of modern zinc coatings.[2] Several available contributions mainly focus on damage processes which take place at large strains.[3,4] However, a thorough investigation of the viscoplastic deformation mechanisms from the early stage of plasticity of zinc coatings to damage initiation is still missing.

The aim of the present work is to investigate the deformation and damage mechanisms of a zinc coating on a hot-dip galvanized interstitial-free steel sheet. Due to the hot-dip galvanizing process, the microstructure of the coating is made of large flat "pancake" zinc grains, with one single grain within the thickness of the coating (8 μm). Several deformation and damage mechanisms including slip, deformation twinning, and cleavage are shown to be active, depending on the loading conditions: tensile, plane-strain, or stamping tests. These observations are made on an as-received material which was temper rolled. For comparison, three other microstructures are also investigated. The first one has not been subjected to the usual temper-rolling treatment, which makes the microstructural observations much easier. The effect of grain size on the coating behavior is an important issue of the present work. That is why a recrystallized coating is investigated, obtained after a recrystallization heat treatment on the as-received material. The in-plane dimension of the zinc grains in the as-received coating is about 600 μm, whereas it is reduced to 30 μm in the recrystallized coating. A reference bulk zinc polycrystalline material, having the same chemical composition as the coating material, is also considered.

The present work is divided into two parts. The first part is devoted to the description and modeling of deformation modes in the four considered microstructures. The companion article[5] deals with the quantitative analysis and modeling of damage after more severe straining. The work is based on careful quantitative microstructural analyses (electron backscattered diffraction (EBSD) orientation-map measurements; determination of active slip systems and twins; and measurements of cleavage-crack density, for different strain paths and loading conditions) and their interpretation using constitutive modeling of crystal plasticity.

Zinc is an hcp metal, and the reader is referred to Reference 6 for the crystallographic description of the hcp lattice and expected deformation modes. The Miller–Bravais notation, including fours indices, is used for hcp structures

RODOLPHE PARISOT, formerly with the Centre des Matériaux, Ecole des Mines de Paris/CNRS, BP 87, 91003-Evry, France, is Director of Maintenance, Air France, 95074 Roissy CDG, France. SAMUEL FOREST, Researcher, ANDRÉ PINEAU, Professor, and FRANÇOIS GRILLON, Researcher, are with the Centre des Matériaux, Ecole des Mines de Paris/CNRS. Contact e-mail: samuel.forest@ensmp.fr XAVIER DEMONET, Research Engineer, and JEAN-MICHEL MATAIGNE, Research Director, are with CED, ARCELOR Recherche et Developpement, BP 39109, 60761 Montataire, France.

Manuscript submitted April 8, 2003.

Table I. Slip Systems in Zinc; the Normal to the Slip Plane and Slip Direction Are Denoted by *n* and *m* Respectively (Notations from Reference 9)

Basal			Prismatic			Pyramidal π_1			Pyramidal π_2			Twinning		
System	*n*	*m*	System	*n*	*m*	System	*n*	*m*	System	*n*	*m*	System	*n*	*m*
BE	(0001)	$[1\bar{2}10]$	EB	$(10\bar{1}0)$	$[1\bar{2}10]$	OE	$(10\bar{1}1)$	$[1\bar{2}10]$	HF	$(2\bar{1}\bar{1}2)$	$[2\bar{1}\bar{1}3]$	ZO	$(10\bar{1}2)$	$[10\bar{1}\bar{1}]$
BF	(0001)	$[2\bar{1}\bar{1}0]$	FB	$(01\bar{1}0)$	$[2\bar{1}\bar{1}0]$	PF	$(01\bar{1}1)$	$[2\bar{1}\bar{1}0]$	IG	$(11\bar{2}2)$	$[11\bar{2}3]$	ZP	$(01\bar{1}2)$	$[01\bar{1}\bar{1}]$
BG	(0001)	$[11\bar{2}0]$	GB	$(\bar{1}100)$	$[11\bar{2}0]$	QG	$(\bar{1}101)$	$[11\bar{2}0]$	JE	$(\bar{1}2\bar{1}2)$	$[\bar{1}2\bar{1}3]$	ZQ	$(\bar{1}102)$	$[\bar{1}10\bar{1}]$
						RE	$(\bar{1}011)$	$[1\bar{2}10]$	KF	$(\bar{2}112)$	$[\bar{2}113]$	ZR	$(\bar{1}012)$	$[\bar{1}01\bar{1}]$
						SF	$(0\bar{1}11)$	$[2\bar{1}\bar{1}0]$	LG	$(\bar{1}122)$	$[\bar{1}123]$	ZS	$(0\bar{1}12)$	$[0\bar{1}\bar{1}1]$
						TG	$(1\bar{1}01)$	$[11\bar{2}0]$	ME	$(1\bar{2}12)$	$[1\bar{2}13]$	ZT	$(1\bar{1}02)$	$[1\bar{1}0\bar{1}]$

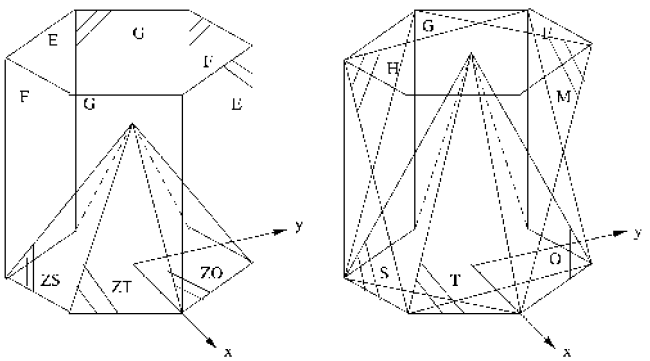

Fig. 1—Two hexagonal unit cells with prismatic and twinning planes (on the left) and pyramidal π_1 and π_2 planes (on the right). Slip and twinning planes are denoted by letters according to Ref. 9 (Table I).

throughout this work. The hcp crystallographic structure of zinc is described by the ratio $c/a = 1.856$. As a result, basal slip is the easiest deformation mode in zinc.[6,7,8] To activate nonbasal slip systems, the crystal must be loaded perpendicular or parallel to the basal plane. The normal to the basal plane is denoted by the *c*-axis. The list of all possible slip planes and the corresponding notations are given in Table I, where *n* stands for the normal to the slip plane and *m* represents the slip direction. The chosen notations for slip and twinning systems are taken from Reference 9. The slip planes are represented in the hexagonal unit cell in Figure 1. The deformation modes actually observed in the zinc coatings considered in this work are basal slip (three systems), pyramidal π_2 slip (six systems), pyramidal π_1 slip (six systems), prismatic slip (three systems), and twinning (six systems).

The four different microstructures are presented in Section II, including composition, grain morphology, crystallographic texture, and EBSD analysis. The mechanical testing procedures are also given in the same section: tensile, plane-strain, and equibiaxial expansion tests. The results reported in Section III deal with the determination of the activated slip and twinning systems, depending on the specific microstructure and grain size and on the loading conditions. The discussion of Section IV presents the two main effects evidenced in this work: the substrate effect, which leads to a strongly biaxial stress state in the zinc grains, and the grain-size effect. Both effects explain the differences in activated slip and twin systems observed for the coatings and the bulk zinc material. The substrate effect is modeled by a simple relaxed-constraint Taylor-like crystal-plasticity model. In contrast, full three-dimensional finite-element simulations of flat-grained and recrystallized coatings are necessary to explain the grain-size effect. Both models and simulations are described in Sections IV–B and IV–C, respectively. The reader is referred to Reference 10 for a detailed description of the basis of the finite-element crystal-plasticity simulations.

Table II. Chemical Composition of the Steel Substrate ($\times 10^{-3}$) (Weight Percent)

C	Mn	P	S	Al	Ni	Ti	Si
1.7	134	12	8	45	14	55	19

II. MATERIALS AND EXPERIMENTAL PROCEDURES

The three different microstructures of the zinc coating are presented in the following subsection, together with a reference bulk zinc material. The experimental mechanical testing methods follow. Finally, the method of identification of activated slip systems combining EBSD measurements and observation of slip traces is described.

A. *Materials*

The substrate of the studied galvanized steel sheet is an interstitial-free steel containing titanium and only 17 ppm carbon in solution. Its chemical composition is given in Table II. The grain size is $d = 10\ \mu$m for a sheet thickness of 0.7 mm.

In the industrial continuous process, the ferritic steel sheet is immersed in a zinc bath alloyed with 0.5 wt pct aluminum and is then cooled under an air stream. This induces the formation of an intermetallic Fe_2Al_5 thin layer which drastically reduces the migration of zinc atoms within the substrate and then inhibits the formation of brittle FeZn compounds.[11,12] This thin layer is responsible for the high strength of the interface.

Three different microstructures of zinc coatings are investigated in this work.

1. *Untempered cold-rolled coating, labeled "NSK"*

Due to the aluminum addition and to iron dissolution in the galvanizing bath, the considered zinc coating is alloyed with a small amount of Al and Fe, according to the solubility of these elements in liquid zinc.[12] After emersion from the bath, the zinc layer is cooled by gas-wiping dies blowing air or nitrogen. Solidification of zinc grains has been shown to start at the steel/coating interface.[13] Figure 2(a) shows the microstructure of the solidified coating. Zinc grains are dendritic and very flat, with a grain size ranging from 200 to

600 μm in the plane of the sheet and with only one grain through the thickness. The coating thickness is 8 $\pm$ 1.5 μm, as deduced from systematic analyses of cross sections shown in Figure 3. Such cross sections are available only for the NSK material.

2. *Tempered cold-rolled coating, labeled "SK"*

In the industrial process, the hot-dip galvanized steel sheets undergo tempered rolling of about 1.3 pct, just after emersion from the galvanizing bath.[2] Figure 2(b) shows the microstructure of the SK coating. The grain size is unchanged when compared to the NSK coating, but many deformation twins are present within the grains.

3. *Recrystallized coating, labeled "recrystallized," or "R"*

A heat treatment of 1 hour at 300 °C applied to the as-received tempered rolled coating leads to a recrystallization process. It results in a small grain coating with still one grain in the thickness, but smaller sizes in the plane of about 30 μm (Figure 2(c)).

In addition to the three previous microstructures, a reference bulk zinc alloy is considered, which has the same chemical composition as the coatings. The liquid zinc alloy is extracted from the same industrial alloyed zinc bath. The samples are obtained by rolling at 200 °C, starting with 15-mm-thick alloyed zinc ingots, to a thickness of 1 mm using 0.5 mm reduction passes. Intermediate annealing treatments are performed at 200 °C. The bulk zinc material is labeled "bulk" in Part II of this article. Its grain size varies from 10 to 70 μm, as seen in Figure 2(d).

B. *Mechanical Testing*

The following mechanical tests have been performed: tensile tests, plane-strain tests on 45 $\times$ 65 mm specimens, and equibiaxial expansion tests on 65 $\times$ 65 mm specimens. The thickness of the samples is 0.7 mm for galvanized steel sheets and 1 mm for the bulk zinc alloy. The rolling direction (RD), transverse direction (TD), and normal direction (ND) are denoted by (1, 2, 3) $\equiv$ (RD, TD, ND) in the following text. Tension tests (in the RD only, in the present article) are performed on a Zwick machine using a 5 kN cell. The gage length and width of the tensile specimens were 75 and 12.5 mm for the NSK and SK materials and 40 and 5 mm for the bulk material. Both plane-strain tests ($\varepsilon_{11} > 0$ and $\varepsilon_{22} \simeq 0$) and equibiaxial-expansion tests ($\varepsilon_{11} = \varepsilon_{22} > 0$) are performed on

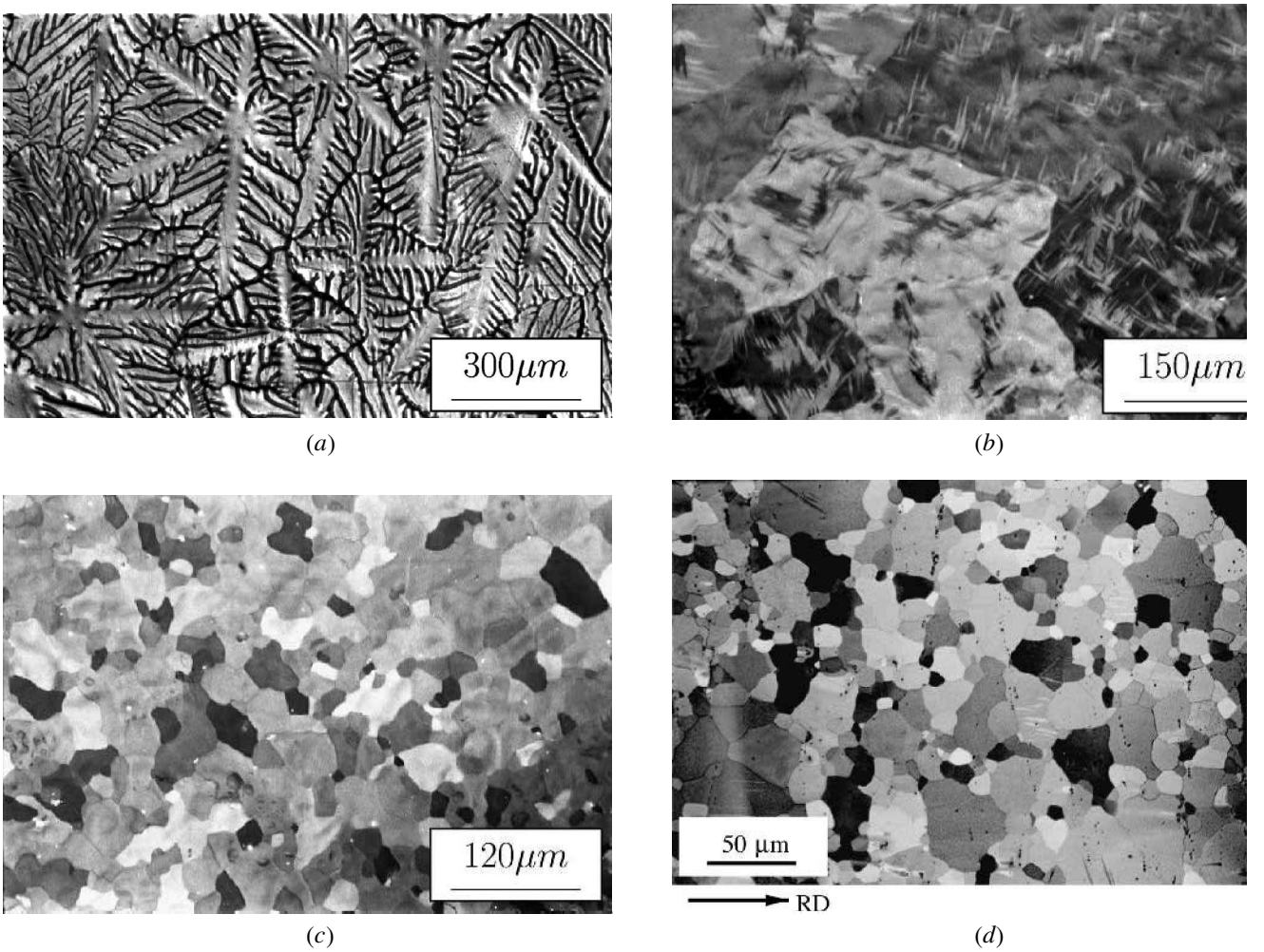

Fig. 2—Microstructures of the four zinc configurations of the study: (*a*) zinc coating, which was not subjected to tempered rolling (NSK); (*b*) rolled tempered zinc coating (SK); (*c*) recrystallized rolled tempered zinc coating (recrystallized); and (*d*) bulk zinc alloy (bulk). The normal to the plane of the figures is direction ND.

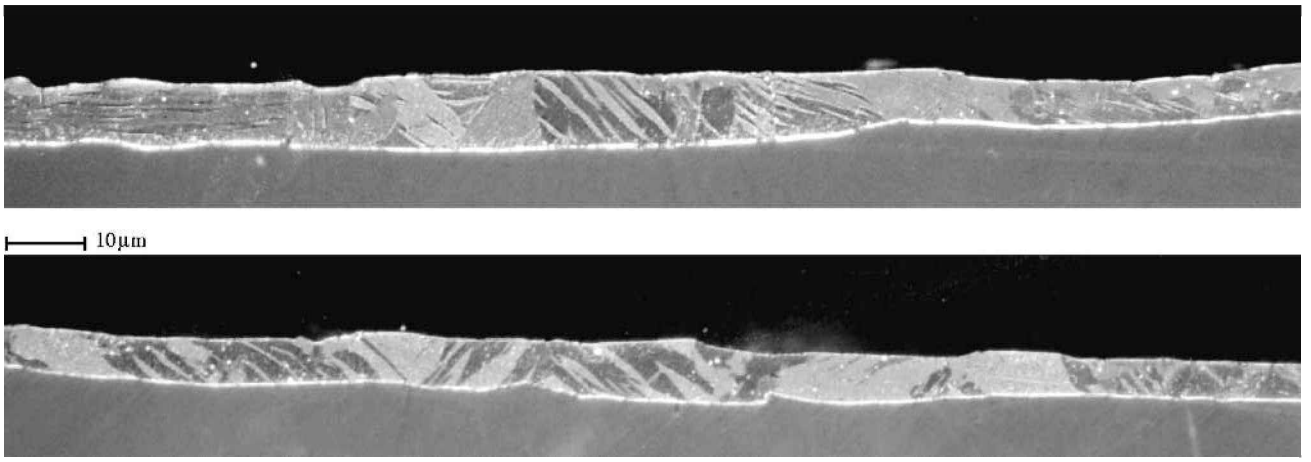

Fig. 3—Two slices of the NSK coating showing that the twins extend over the entire thickness of the coating (polarized light micrographs, mean thickness of the coating: 8 μm, the steel substrate is the lower gray layer).

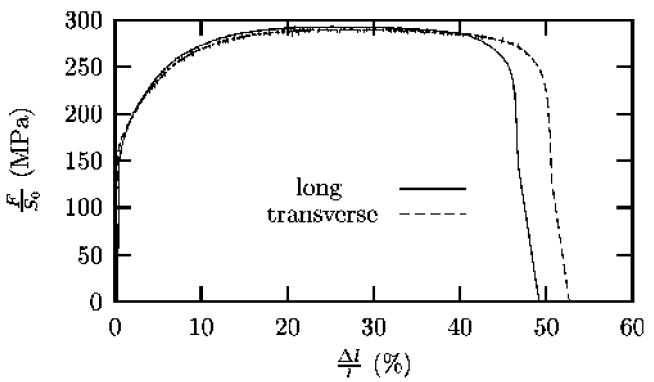

Fig. 4—Tensile behavior of the coated IF steel SK (strain rate $\dot{\varepsilon} = 0.002\ s^{-1}$): rolling direction RD (long) and transverse direction (transverse).

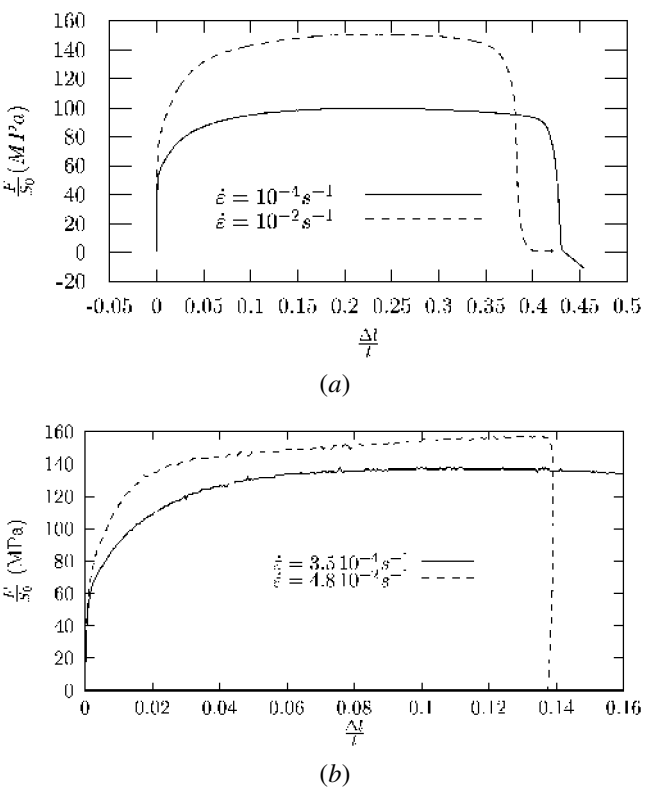

Fig. 5—Tensile behavior of the bulk zinc alloy: (*a*) tension along the rolling direction and (*b*) along the transverse direction for two different strain rates at room temperature.

an Erichsen stamping machine. Strains are measured after the test, looking at the deformation of a network of 3-mm-diameter chemically etched circles deposited before the test. The strain rate cannot be measured precisely on the Erichsen machine: only the mean strain rate is known. The strain rate is $\dot{\varepsilon} = 10^{-4}\ s^{-1}$ for tension, plane-strain, and expansion tests.

The tensile response of the SK-coated steel at room temperature is given in Figure 4 and coincides with that of the substrate.[10] Note that the lateral deformation could also be measured for tensile tests in the RD and TD, in order to estimate the strain anisotropy of the steel sheet and its Lankford coefficient. Figure 5 shows the anisotropic and strongly rate-sensitive tensile response of the bulk zinc alloy at room temperature. It should be remembered that room temperature corresponds to a relative temperature of 0.42, since the melting temperature of pure zinc is 419 °C.

In all micrographs shown in the this article, the main loading axis is horizontal.

C. *Texture Analysis*

The three considered coating and bulk materials have different crystallographic orientation-distribution functions, due to very different processing conditions. An extensive EBSD analysis was carried out for each material. The corresponding pole figures are shown in Figure 6.

The coatings are strongly anisotropic, with most zinc grains having their *c*-axis normal to the sheet plane (Figures 6(a) through (c)). This is due to the hot-dip solidification process. Tempered rolling leads to the local formation of many small deformation twins (Figure 2(b)). Twinning implies a rotation of the lattice, which is of 86.04 deg for the *c*-axis in zinc with respect to a $<10\bar{1}0>$ axis.[14] However, the texture of the SK coating is only slightly different from that of the NSK

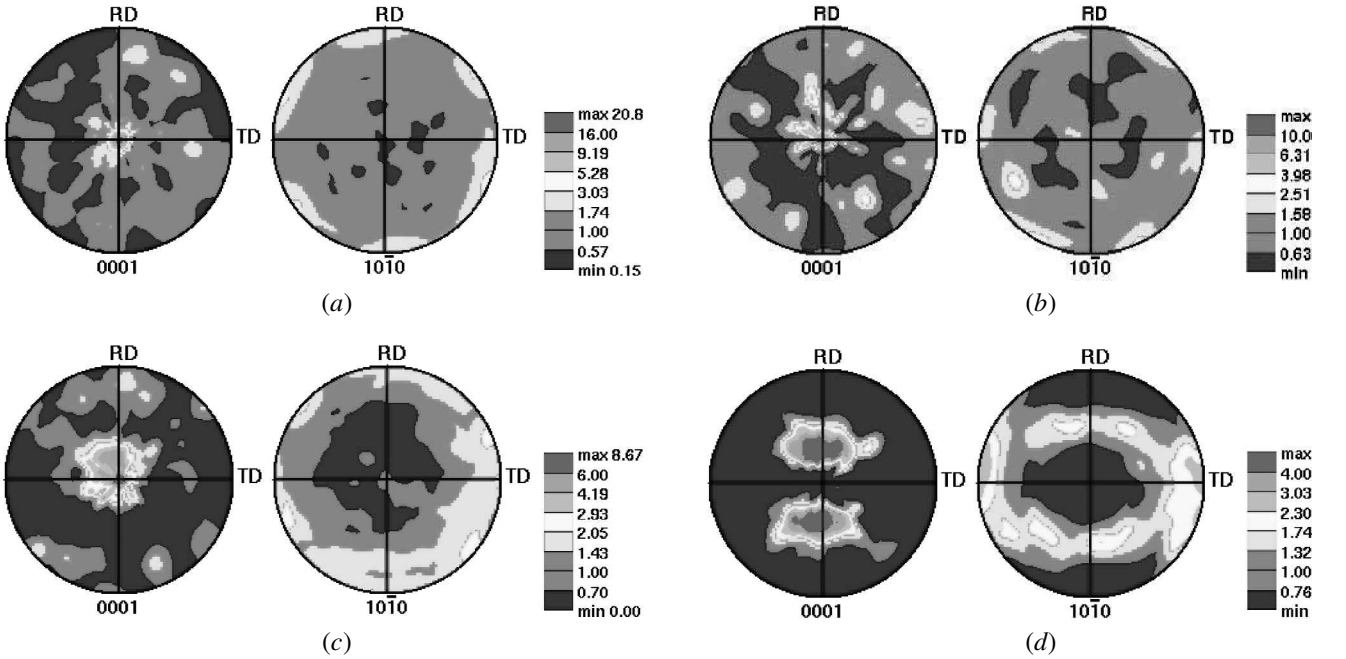

Fig. 6—Crystallographic textures of the investigated materials; pole figures for the zinc coatings: (*a*) NSK, (*b*) SK, (*c*) recrystallized, and (*d*) bulk zinc alloy.

coating (Figure 6(b)). Finally, the recrystallization process does not significantly affect the texture of coating R, as observed in Figure 6(c). Since the bulk alloyed zinc has been subjected to rolling, it exhibits the classical zinc sheet texture reported in Reference 15, with a *c*-axis tilted 25 deg in the RD (Figure 6(d)).

D. *The EBSD Analysis and Determination of the Deformation Modes*

The EBSD technique is extensively used in this work to obtain local orientation maps of groups of 20 to 80 grains. The EBSD system used in this work is built in a field-emission scanning microscope and includes an analogic close-coupled device camera with on-chip integration (Hjelen-type): the voltage and current are 20 kV and 0.1 mA, respectively; the working distance is 19 mm; and the tilt angle is 70 deg. Finally, the data are treated using OIM software by TSL. Other details on the used EBSD technique are to be found in Reference 16. Orientation maps of the NSK coating and of the bulk material are presented in References 10 and 17 and are, therefore, not reported here. Optical observations of the same investigated zones reveal the presence of slip lines and twins after straining (Figure 7). The combination of EBSD and optical observations is used to determine the nature of the activated slip and twinning systems as follows.

The EBSD analysis is carried out before material testing and at different steps of interrupted-tension plane-strain and expansion tests. Each grain of the investigated zone is labeled by a letter system (A, B, C, . . . , AA, AB, AC, . . .) and its orientation is recorded. Some of the indexed grains can be seen in Figures 7(a), (c) and (d). These letters are used to show the orientation of the tensile axis in the inverse pole figures of Figures 10 through 12. It is, therefore, possible to establish the sequence of activation for different slip-system families.

In each case, the orientation of the slip lines is compared to the orientation of the trace of expected basal, prismatic, and pyramidal slip planes. Since several slip planes may have a very close intersection with the plane of the sheet, the interpretation can be ambiguous, as already indicated in Reference 17. However, more than 50 pct of the slip lines could be unambiguously determined. Except for basal slip, there is one slip direction per slip plane for hcp crystals (*e.g.*, six pyramidal π_2 slip systems for six slip planes), so that, in this case, the slip system is identified once the slip plane is known. The identification of the twinning system is always possible, since the orientations of the twinned and parent crystal are determined by EBSD.

III. RESULTS

The observed deformation modes are presented successively for the four considered materials. The interrupted tests enable one to establish the chronology of slip and twinning activation. Attention is drawn also to the difference in the observed deformation mechanisms according to the uniaxial (tension) and multiaxial (plane-strain and expansion) overall loading conditions. In the present article, we concentrate on relatively small strains (about 10 pct), which corresponds to the situation met during metal forming. This means that no dynamic recrystallization takes place during the tests reported in this work, in contrast to the situation observed at larger strains.[17]

A. *NSK Coating*

As an example, a zone of 27 grains of the NSK coating is investigated, combining optical observations and EBSD analysis for an interrupted tensile test conducted up to 10 pct overall deformation. Four grains out of 27 can be seen in Figure 7(a). After $\varepsilon_{11} = 1.5$ pct in tension along the RD,

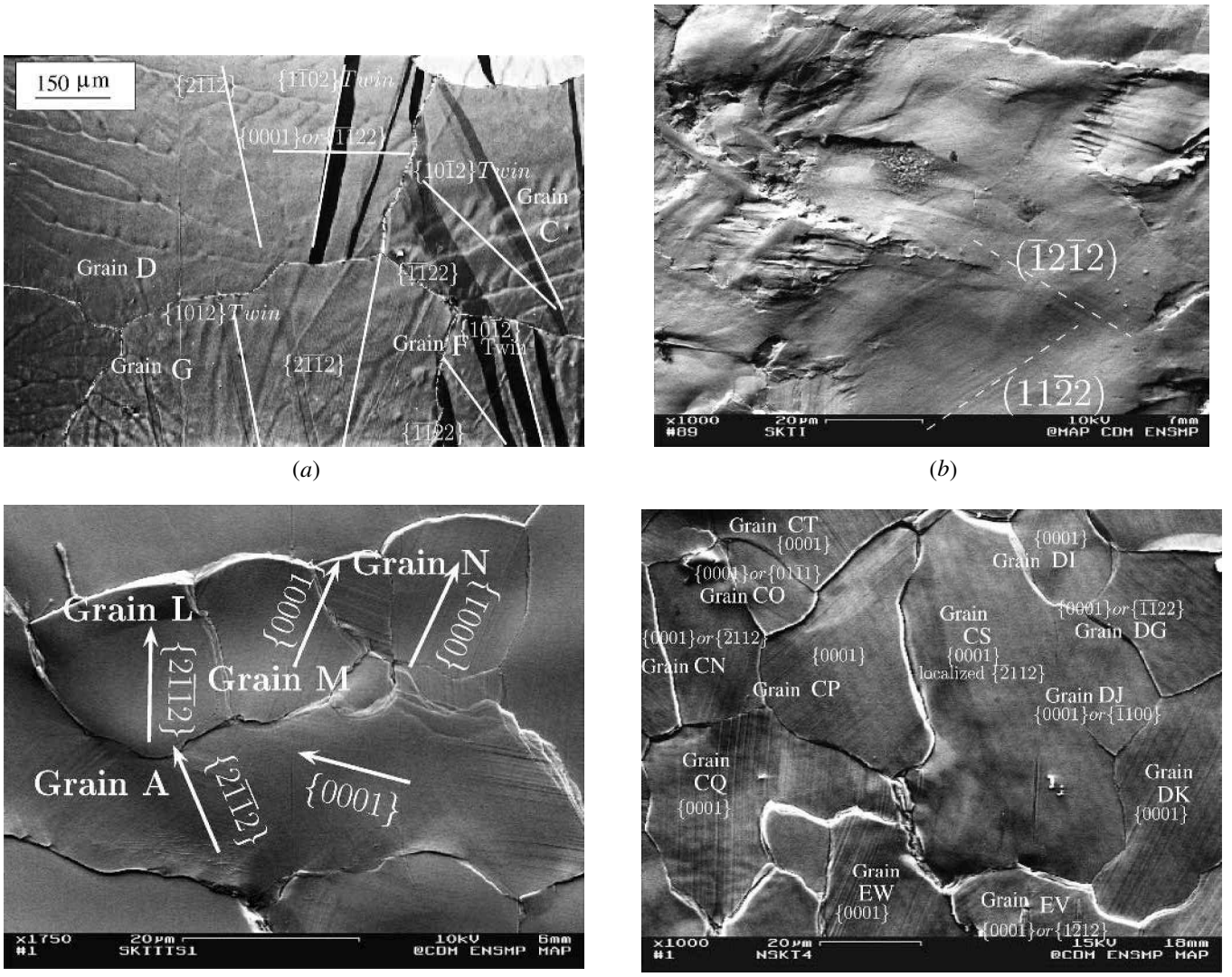

Fig. 7—Identification of activated slip systems in tension along the horizontal direction: (*a*) NSK coating after 2.5 pct tensile strain, (*b*) SK after 2.5 pct tensile strain, (*c*) recrystallized coating after 2.5 pct tensile strain, and (*d*) bulk zinc after 4 pct tensile strain.

all the grains exhibit at least two active deformation modes, with an average of 1.6 activated slip systems and 1 twinning system per grain (Figure 7(a)). After $\varepsilon_{11} = 2.5$ pct, the statistics have not significantly changed: 1.8 activated slip systems and 1.1 twinning systems per grain (note that we do not count the number of individual twins, but the number of activated twinning systems). At this strain level, slip lines are also visible in the reoriented crystal within some twins. At larger strains, these deformation modes pertain. Twinning remains significantly active, and twins can spread over entire grains at $\varepsilon_{11} = 10$ pct.

Nonbasal slip turns out to play an important role in the deformation of the NSK coating, since two or more different slip planes are found systematically in the deformed grains. More than that, basal slip is far from being the main slip mechanism. Pyramidal π_2 slip was identified at 28 locations among the grains for $\varepsilon_{11} = 4$ pct, and pyramidal π_1 and prismatic slip were identified at 14 locations (but only three times without ambiguity), whereas basal slip appeared only eight times. By "slip location," we mean a bundle of parallel slip lines.

A special double-slip configuration is frequently observed in the strained NSK coating. It is called here "chevron," because of its shape. Several chevrons can be seen in Figure 8(a). It is associated with the interaction of two pyramidal π_2 slip systems which are symmetrical with respect to the *c*-axis. Such a mechanism is not reported in the literature, to the authors' knowledge. Figure 8(b) gives a possible mechanism for the formation of a chevron. Knowing the grain and slip-line orientations, the corresponding slip planes can be identified and are found to be pyramidal π_2 planes. The corresponding glide direction can be deduced, since one pyramidal π_2 slip plane is associated with one slip direction only. Edge dislocations only are considered, following References 18 and 19. The Burgers vectors of the dislocations belonging to the two activated slip systems are of the form $\boldsymbol{c} + \boldsymbol{a}$ and $\boldsymbol{c} - \boldsymbol{a}$. They can form attractive junctions with a resultant Burgers vector of $2\boldsymbol{c}$ which are sessile and induce a local hollow, as seen in Figure 8(a) at the intersection of the slip lines.

Twinning also is a major deformation mode observed during tension tests of the NSK coating. Figure 9 shows

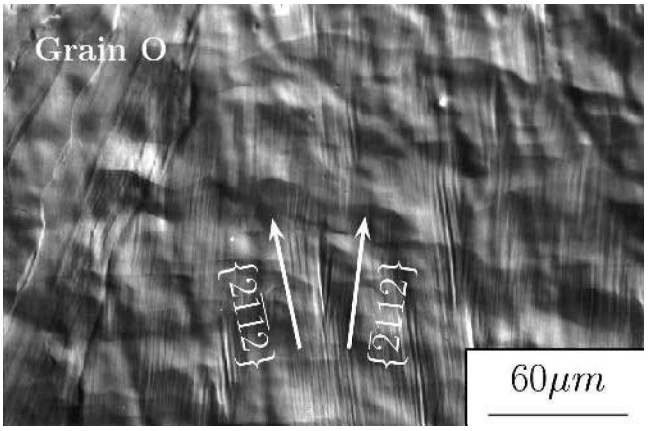

(*a*)

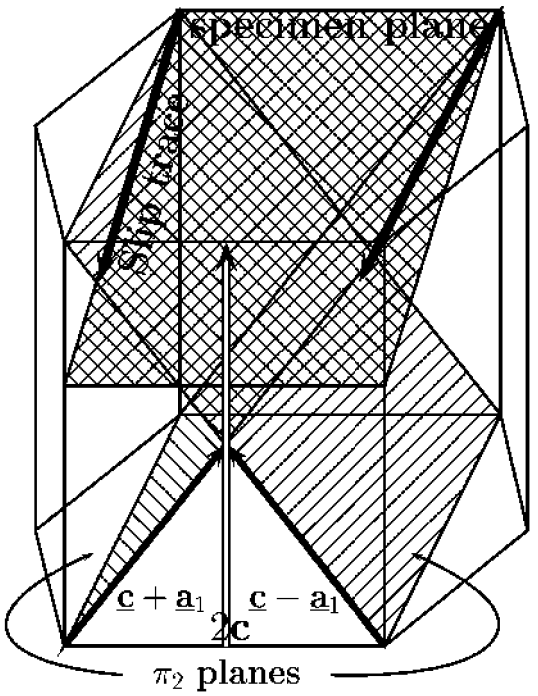

(*b*)

Fig. 8—Formation of a chevron following the interaction of two pyramidal π_2 slip systems, which are symmetrical with respect to the *c*-axis (NSK coating): (*a*) polarized light micrograph and (*b*) proposed mechanism.

the sequence of twin formation and propagation in a grain for an interrupted tension test. When ε_{11} varies from 0 to 7.5 pct, many twins nucleate on the previously virgin coating: these thin twins cross the entire section of the grains. Twins nucleate at the grain boundaries and at defects like indentation points present as reference marks. Two twinning systems are usually activated, being symmetric with respect to the tension axis, which is horizontal in Figure 9. After $\varepsilon_{11} = 7.5$ pct, twins do not nucleate any more. Instead, the previous twins grow laterally and spread over the entire grain. At $\varepsilon_{11} = 22$ pct, the central grain of Figure 9 is almost entirely twinned. This mechanism is observed for all twinned grains of the NSK coating. Views of the coating along the thickness (Figure 3) show that the twins are inclined with respect to the tensile axis and cross the whole thickness. Some lenticular twins stop at the interface coating/substrate, but others can then extend laterally.

The results in tension are summarized in the inverse pole figure of Figure 10(a), which shows the domains of grain orientation associated with basal slip, pyramidal π_2 slip, twinning, and the formation of chevrons.

A similar analysis of interrupted plane-strain and expansion tests shows that the deformation modes are basically the same as in tension. This can be seen in the inverse pole figures (Figures 10(b) and (c)). However, the number of activated slip systems per grain is larger. In grains having their *c*-axis close to the normal sheet direction, three different slip-line bundles forming equilateral triangles are frequently observed, especially for expansion tests. Pyramidal π_2 slip remains the main active deformation mode of the NSK coating. The surface fraction of twinned crystals increases with the multiaxial state. The hatched zone of Figure 10(c) indicates a large domain of twin activation.

B. *SK Coating*

The mechanical behavior of the SK coating is almost identical to that of the NSK coating. Observations of the coating are much more difficult to make, because of the rough skin-passed surface and the presence of numerous small twins (Figure 7(b)). However, the nucleation stage of deformation twinning is reduced, since small twins are already present in this microstructure before any subsequent deformation and act as nuclei for further twinning. Because of this fragmented microstructure, the deformation modes are more complex but do not significantly deviate from those presented in Figure 10 for the NSK coating. Pyramidal π_2 slip lines can be seen in Figure 7(b). Several slip systems are seen within the small initial twins after deformation. However, the twins have not been shown to influence significantly the activation of the slip systems in the parent crystal. That is why the quantitative analysis of slip-system activation has not been performed for the SK material.

C. *The Recrystallized Coating*

The ratio *d*/*h* of the mean grain diameter in the plane of the sheet (*d*) divided by the coating thickness (*h*, equal to 10 μm) varies from 60 for the NSK coating to 3 for the recrystallized coating. This parameter strongly affects the deformation modes observed at the free surface of the coating. However the grain-size distribution in the sheet plane is much more heterogeneous for the recrystallized coating than for the NSK or SK materials. In the smallest grains, basal slip is found to be the main deformation mode. Basal slip is quite homogeneously distributed in the grain, whereas nonbasal slip takes place preferentially near the grain boundaries (refer to grains M and N in Figure 7(c)). For larger grains (grain L of Figure 7(c)), the situation becomes similar to that encountered for the NSK coating. Grains larger than $d = 100$ μm display the same behavior as in the NSK coating.

After $\varepsilon_{11} = 4$ pct, basal slip represents 56 pct of the slip-line bundles observed on a map of 87 investigated grains. Pyramidal π_2 slip represents 44 pct of the observed slip-line bundles, which are preferentially found close to the grain boundaries. No twinning is observed at this strain level in spite of the strongly basal texture. Figure 11 shows the identified deformation modes reported in inverse pole figures for tension, plane-strain, and

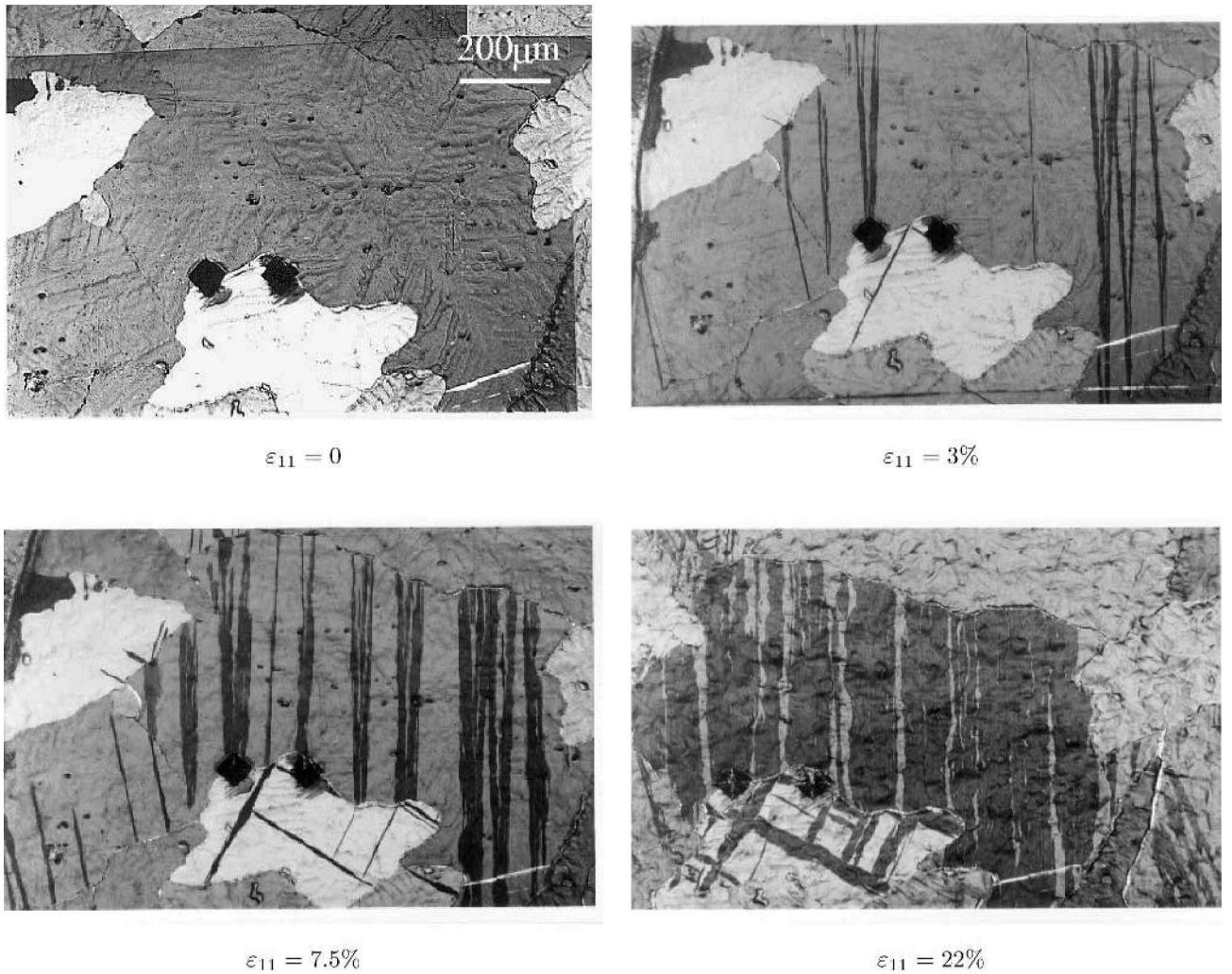

Fig. 9—Kinetics of twinning during a tension test on the NSK coating; polarized light micrographs (two indentation prints are visible at the image center).

expansion tests. The arrows indicate the displacement of the boundary of the activation domains when the grain size decreases. The main difference with respect to the NSK and SK coatings is the absence of chevrons and strongly reduced twinning.

D. *Bulk Zinc Alloy*

Interrupted tests were also performed for the reference bulk zinc alloy. A zone of 103 grains of bulk zinc was investigated in tension. After $\varepsilon_{11} = 1.2$ pct in tension along the RD, an average of 1.1 activated slip systems per grain is observed without any twin. After $\varepsilon_{11} = 4$ pct, only 34 grains out of 103 display double slip. This newly activated slip system remains weak and is observed mainly in the vicinity of grain boundaries (Figure 7(d)). Even the grain CS of Figure 7(d), for which the angle (*c*, ND) is 16 deg, deforms by basal slip. At this strain level, two twins are observed. On average, 55 pct of the slip lines of the bulk material are due to basal slip. It appears that 21 pct more slip traces may be basal slip, but the determination is ambiguous. Therefore, 24 pct of the slip-line bundles indicate undoubtedly nonbasal slip: these lines are localized close to the grain boundaries. Pyramidal π_1 slip systems and prismatic slip systems are counted, respectively, once and twice.

The observations are summarized in the inverse pole figures shown in Figure 12(a). Basal slip occupies the major part of a standard triangle. Furthermore, its activity spreads over the pyramidal π_2 domains. In contrast, the boundaries of deformation domains of the NSK material are well defined.

In the case of multiaxial loading, basal slip remains the dominant deformation mechanism of the bulk zinc alloy. Pyramidal π_2 slip and twinning remain very limited.

E. *Summary of Results*

Three main deformation modes have been identified in the four investigated microstructures: basal slip, pyramidal π_2 slip, and twinning. Pyramidal π_1 and prismatic slip are scarcely observed. The NSK and SK materials and the large grains of the recrystallized coating display a similar behavior, for which pyramidal π_2 slip and twinning are the dominant deformation modes. In contrast, the recrystallized coating and the bulk material display mainly basal slip, this result being not affected by the application of multiaxial loads. The quantitative results of slip and twin activity in the four materials are summarized in Table III. For plastic slip, the percentage reported in the table gives the ratio of the number of identified slip-line

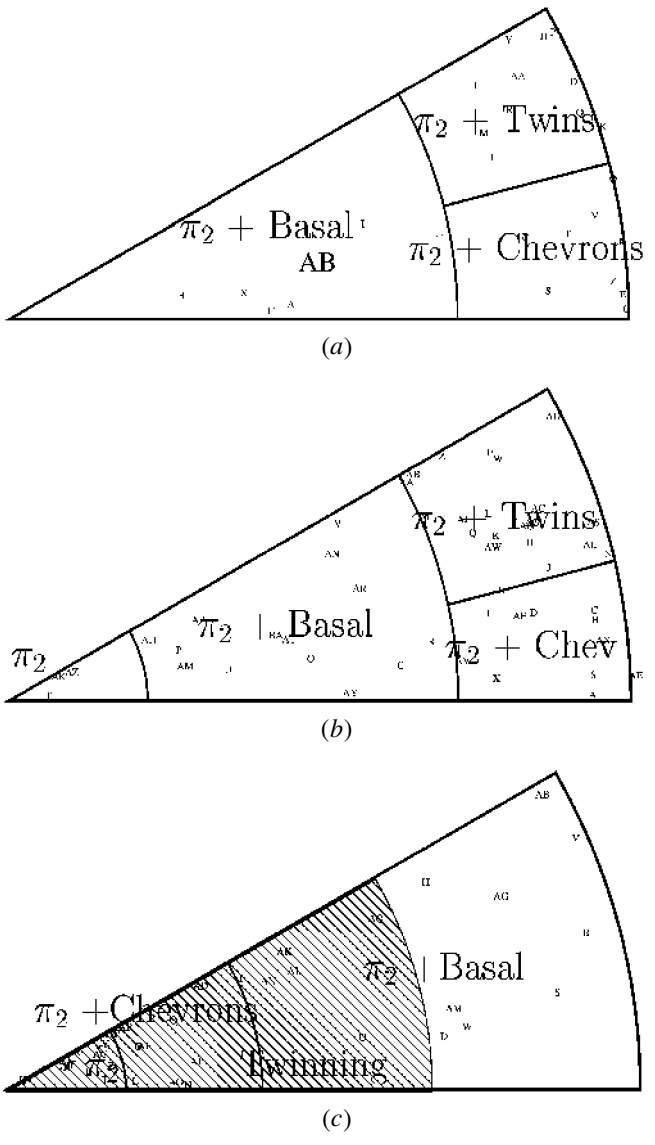

Fig. 10—Inverse pole figures giving the tensile direction of many grains and the corresponding zones of slip activity; NSK zinc coating subjected to (*a*) tension, (*b*) plane strain test, and (*c*) equibiaxial expansion test (in this case, the plotted direction is the direction normal to the coating). The single and double letters indicate individual grains, the orientations of which have been identified using EBSD technique. Some of the grains can be seen in Fig. 7. The hatched zone corresponds to a domain of intense twinning.

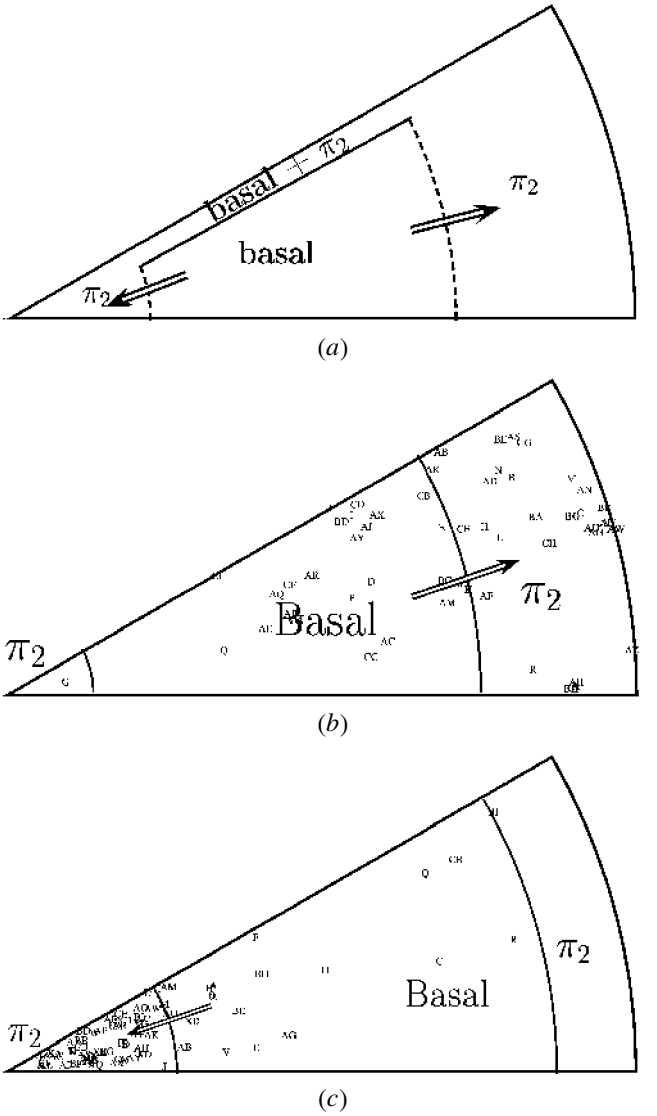

Fig. 11—Inverse pole figures giving the tensile direction of many grains and the corresponding zones of slip activity. Recrystallized zinc coating subjected to (*a*) tension, (*b*) plane strain test, and (*c*) equibiaxial expansion test (in this case, the plotted direction is the direction normal to the coating). The single and double letters indicate individual grains, the orientations of which have been identified using EBSD technique. Some of the grains can be seen in Fig. 7. The arrows indicate the translation of the domain boundary when grain size is decreased.

bundles corresponding to a given slip system divided by the total number of identified bundles. Regarding twinning, individual twins inside the grains are not counted. One activated twinning system is counted only once in each grain.

IV. DISCUSSION AND MODELING

A. *Substrate and Grain-Size Effects*

Two main features of the deformation of zinc coatings can be deduced from the previous results.

1. The deformation modes of the NSK and SK coatings are strongly different from that of bulk zinc. Numerous slip and twinning systems are activated during the deformation of the coatings, whereas the deformation of bulk zinc involves mainly basal slip, as expected from the literature.[20,21] Calculations based on crystal plasticity, presented in the next subsection, show that the difference in crystallographic textures of the zinc coating and bulk material is not the only origin of the present effect. We call it the *substrate effect.*
2. The deformation modes of the recrystallized coating and bulk zinc are very similar. This happens when the ratio *d*/*h* decreases to 3 or less. This is the evidence of a *grain-size effect.* The constraining-substrate effect seems to be active only for pancake grains and not for equiaxed grains any more.

The two following subsections provide a quantitative analysis of both phenomena.

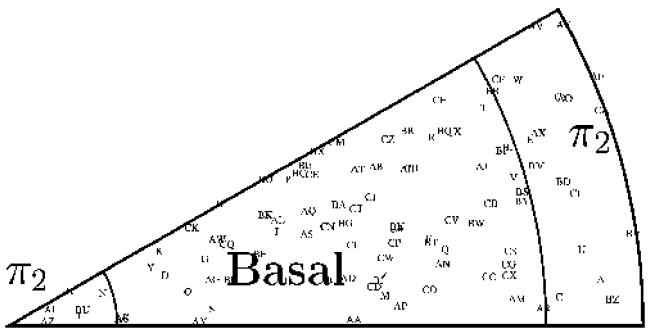

(*a*)

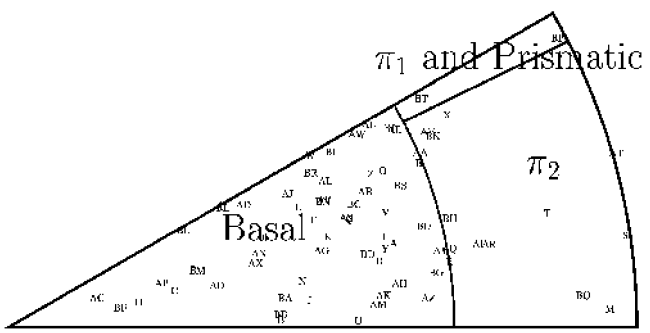

(*b*)

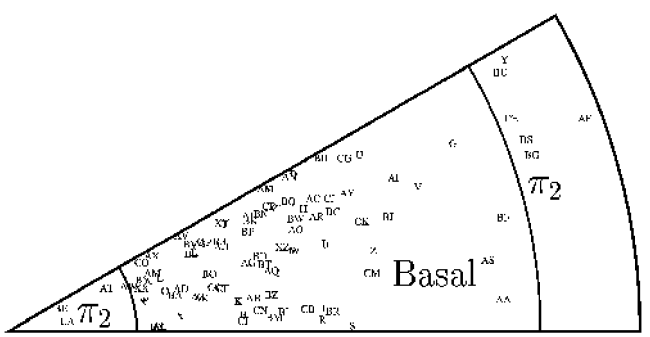

(*c*)

Fig. 12—Inverse pole figures giving the tensile direction of many grains and the corresponding zones of slip activity. Bulk zinc subjected to (*a*) tension in rolling direction, (*b*) plane strain test, and (*c*) equibiaxial expansion test (in this case, the plotted direction is the direction normal to the coating). The single and double letters indicate individual grains, the orientations of which have been identified using the EBSD technique.

B. *Relaxed-Constraint Taylor-like Modeling*

Models based on crystal plasticity are available to simulate the mechanical behavior of zinc. In Reference 22, for instance, a so-called self-consistent polycrystal model is used to calculate the deformation and texture evolution of bulk polycrystalline zinc. In the case of the pancake grains of the NSK coating, the relaxed-constraint Taylor-like models initially proposed in References 23 and 24 are more relevant. All these models assume that the grain behavior is described by a set of constitutive equations accounting for crystal plasticity.[25] The plastic strain rate is the sum of the contribution of all activated slip systems, according to

$$\varepsilon_{ij}^{p} = \sum_{s=1}^{N} \frac{\dot{\gamma}^{s}}{2} \left(m_i^s n_j^s + n_i^s m_j^s\right) \qquad [1]$$

where γ^s is the amount of slip for the slip system s. It is recalled that the slip direction and normal to the slip plane are denoted by m_i^s and n_j^s, respectively. The total number of considered slip systems is N. The criterion for the activation of slip system s is Schmid's law:

$$\tau^s = m_i^s \cdot \sigma_{ij} \cdot n_j^s = r^s \qquad [2]$$

where r^s is the current critical resolved shear stress (CRSS). A viscoplastic flow rule is adopted, which eliminates the problem of possible indeterminacy of activated slip systems[23] and which is necessary for zinc tested at room temperature, as shown in figure 5.

$$\dot{\gamma}^{s} = \max\left(0, \left(\frac{|\tau^s| - r^s}{K}\right)^{n}\right) \text{sine}\,(\tau^s) \qquad [3]$$

An explicit nonlinear isotropic hardening rule is used:

$$\tau^s = \tau_0^s + Q^s \sum_{r=1}^{N} H^{sr}\left(1 - \exp\left(-b^r \gamma_{\text{cum}}^r\right)\right) \qquad [4]$$

The initial threshold is τ_0^s, and the matrix H^{sr} accounts for self- and latent hardening, *i.e.*, interaction between one slip system and all slip systems. The cumulative amount of slip (γ_{cum}^s) is computed from $\dot{\gamma}_{\text{cum}}^s = |\dot{\gamma}^s|$. The coefficient b^s represents the saturation rate of hardening (Q^s). A more detailed presentation of the model is given in the Appendix. Note that the presented constitutive framework is restricted to the case of small strains, which is the case in the presented simulations.

Table III. Deformation Modes of Two Analyzed Zinc Coatings and the Bulk Zinc Material Experimentally Obtained for Tension, Plane Strain, and Equibiaxial Expansion Tests (Values Are Given for 4 Percent Equivalent Plastic Strain)

Loading	Material	Basal	Pyr.π_2	Twinning	Pyr.π_1	Prismatic	Pole Figures
Tension	NSK	15 pct	52 pct	26 pct	6 pct	1 pct	10(a)
	R	56 pct	44 pct	—	—	—	11(a)
	Bulk	70 pct	27 pct	—	1 pct	2 pct	12(a)
Plane strain	NSK	11 pct	50 pct	36 pct	2 pct	1 pct	10(b)
	R	30 pct	59 pct	8 pct	2 pct	—	11(b)
	Bulk	73 pct	25 pct	—	2 pct	—	12(b)
Equibiaxial expansion	NSK	9 pct	48 pct	38 pct	3 pct	2 pct	10(c)
	R	14 pct	81 pct	1 pct	3 pct	1 pct	11(c)
	Bulk	84 pct	10 pct	2 pct	1 pct	1 pct	12(c)

The material parameters r_0^s, Q^s, H^{rs} and K^s, n^s have been identified for the basal, pyramidal π_1 and π_2, and prismatic slip-system families of zinc single-crystalline zinc. The case of twinning is dealt with as a slip system with a corresponding critical resolved shear stress. Lattice reorientation is not accounted for in this model. The entire identification procedure is presented in Reference 10. The found parameters and detailed expression of the interaction matrix are given in the Appendix. Here, we simply insist on the hierarchy of slip systems: the basal slip-system family has the lowest initial CRSS ($\tau_0 = 1.5$ MPa), pyramidal π_2 comes next with $\tau_0 = 15$ MPa, and, finally, pyramidal π_1 ($\tau_0 = 20$ MPa), prismatic slip ($\tau_0 = 22$ MPa), and twinning ($\tau_0 = 25$ MPa) follow. Note also that elasticity is also taken into account *via* the elastic-strain tensor $\boldsymbol{\varepsilon}^e = \boldsymbol{\varepsilon} - \boldsymbol{\varepsilon}^p$. The strongly anisotropic elastic moduli of single-crystalline zinc are introduced for that purpose (Reference 10 and the Appendix). The determined value of the strain-rate sensitivity is $n = 5$ for all slip-system families, in agreement with Reference 26. The value of parameter K is 1 MPa·s$^{1/n}$ for basal slip and 10 MPa·s$^{1/n}$ for pyramidal π_2 slip systems.

The relaxed-constraint Taylor model is now applied to the individual pancake grains of the NSK coating for a given mechanical test, as follows.

1. Compute the deformation state of the steel substrate subjected to the overall loading conditions of the test (tension, plane-strain, or expansion test). For that purpose, a constitutive model for the substrate is needed. A classical elastoplastic model with an anisotropic Hill yield criterion is used. The identification of this model and the obtained parameters can be found in Reference 10.
2. Call E_{11}, E_{22}, and E_{12} the strain components of the substrate in the RD and TD, during the test.
3. Prescribe these strain components to individual zinc single crystals having the orientations of some grains of the coating measured by EBSD:

$$\varepsilon_{11}^X = E_{11}, \varepsilon_{22}^X = E_{22}, \varepsilon_{12}^X = E_{12}$$

at each loading time. The components of the imposed deformation of individual grains are denoted by ε_{ij}^X. For the loading conditions to be complete for each single crystal, one has to add the conditions corresponding to the relaxed-constraint Taylor model:

$$\sigma_{33} = \sigma_{13} = \sigma_{23} = 0$$

The constitutive Eq. [1] through [4] are used to compute the activated slip systems and the corresponding stress response. They are integrated along the loading path using an implicit Newton integration scheme.[27]

In this model, it is assumed that the substrate dictates its deformation to the pancake grains except in the ND 3, which remains free of forces. Accordingly, the pancake grains are handled as individual single crystals. The interaction between neighbouring grains is neglected in the present model.

The model is applied first to the case of tensile loading. The main information provided by the simulations carried out for several pancake grains is that tension for the substrate does not mean a tensile stress state in the individual zinc grains. On the contrary, a strongly biaxial stress state (σ_{11}, σ_{22}) is found in the pancake grains for tension in direction 1, for instance. This is due to the strong plastic anisotropy of the zinc grains and can be explained as follows. In tension, if the substrate undergoes the tensile deformation $E_{11} = 1$ pct, the lateral deformation E_{22} is then about 0.5 pct. When this deformation is imposed to a zinc single crystal, it results in a strongly biaxial stress state (σ_{11}, σ_{22}), because, for the investigated crystal orientations, no combination of slip systems can lead to a plastic-flow ratio ($\varepsilon_{22}/\varepsilon_{11}$) identically equal to $-1/2$. This is necessarily associated with considerable stresses (σ_{22}). For certain orientations corresponding to the *c*-axis close to the sheet ND, we found $\sigma_{22} \simeq -3\sigma_{11}$. This biaxial stress state inevitably results in multiple non-basal slip. Figure 13 shows the results in the case of the grain AB, the orientation of which is given in the inverse pole figure of Figure 10(a). This grain is perfectly oriented for basal slip for a tension state. Instead, three slip systems are observed experimentally: two pyramidal π_2 and one pyramidal π_1. Figure 13(a) shows that the relaxed Taylor model predicts the right combination of activated slip systems. Actually, this grain cannot accommodate the tensile deformation of its substrate, only by basal slip. A biaxial stress state with strong compressive stress (σ_{22}) is found again. The model predicts a very low amount of basal glide, which is in accordance with the fact that no basal slip lines were observed. Moreover, Figure 13(b) shows that the model predicts the activation of the slip planes $(\overline{1}122)$ and $(2\overline{1}12)$, in agreement with the observed slip lines.

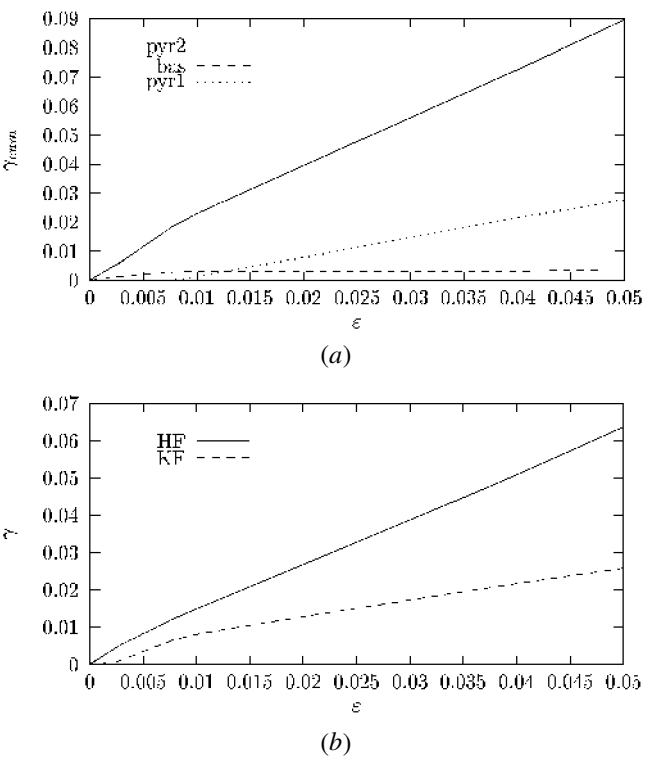

Fig. 13—Application of a relaxed contraint Taylor-type model to the grain AB, the orientation of which is given in Fig. 10(a), after $\varepsilon_{11} = 5$ pct in tension: (*a*) cumulative slip for all activated slip system families and (*b*) activated pyramidal π_2 slip systems; γ denotes the amount of slip for each slip system, and the names HK and KF refer to the names of pyramidal slip systems taken from Ref. 9 (Table I).

The model turns out to be able also to describe accurately the response of the NSK coating pancake grains under equibiaxial loading of the steel sheet. Even more slip systems and twinning are predicted than for tension, in accordance with the results of Table III.

Finally, the same methodology has been applied to the more equiaxed grains of the recrystallized coating. Since the model does not incorporate explicitly the effect of the ratio *d*/*h* nor any other length scale, and since the texture is not strongly different from that of the NSK coating, the model provides the same results as previously. It is unable to explain the different mechanical behaviors observed for the NSK and recrystallized coatings. That is why a more refined model is proposed in Section C. The microstructure of the coating must be taken into account in a more explicit way in order to explain the differences observed between both conditions.

C. *Multicrystalline Modeling*

The so-called multicrystalline approach takes the actual geometry and orientation of a cluster of grains into account. This approach has been used in Reference 28, for instance. For that purpose, a real microstructure of an *in-situ* tensile specimen of NSK galvanized sheet, tested in the scanning electron microscope (SEM) chamber, was analyzed by both EBSD and polarized-light microscopy. From this analysis of the central area of 3.7 mm (length) × 1.5 mm (width), a two-dimensional finite-element mesh was designed. It distinguishes 34 sets of elements to represent the 34 grains of the specimen. The crystal orientations of the 34 grains are representative of the texture of the NSK coating and are given in Reference 10. A three-dimensional mesh is obtained by translation of the two-dimensional mesh in the ND, assuming that the grain boundaries are perpendicular to the sheet plane. The actual *d*/*h* ratio is, therefore, introduced explicitely in the modeling. Four layers of elements are piled up for meshing the coating in the thickness direction, while only one layer is used for meshing the substrate in the thickness. The three-dimensional mesh is made of 5145 bricks, which corresponds to 37,170 (reduced) integration points with 5646 nodes for the linear elements. The following boundary conditions are applied in order to simulate the *in-situ* tensile test in the rolling direction: displacement $U_3 = 0$ on the midsteel plane (x_1, x_2), displacement U_1 is prescribed on the two end planes (x_2, x_3), and other planes are left free of forces.

The computation for the ratio $d/h \simeq 60$ corresponding to the NSK coating is presented in more detail in Reference 10, where the comparison with *in-situ* experiments can also be found. A tensile test up to $E_{11} = 1$ pct was simulated. The results of the analysis presented therein can be summarized as follows.

1. The coating thickness is too small for significant strain and stress gradients to develop from the interface to the free surface.
2. The constraining effect of the substrate has been proven to lead to strongly biaxial stress states in the zinc grains.

The latter result has been reproduced by the much-more-simple relaxed-constrained Taylor model used in Section B. The complete computation, however, justifies *a posteriori* the assumptions of the relaxed-constraint Taylor model in the special case $d/h = 60$.

The advantage of the numerical simulation is that it can be carried out again for a different value of the ratio *d*/*h* in order to isolate the direct influence of this parameter on the behavior of the coating. The topology of the 34 grains is kept unchanged, but the thickness of the mesh of the coating is changed to reach the value $d/h = 3$, corresponding to the recrystallized coating. Figure 14 shows the corresponding finite-element mesh. A tensile test is simulated again with this new configuration. The overall tensile curve is, of course, unchanged, because of the same main contribution of the steel substrate. However, the stress/strain within the grains is found to be very different from the NSK configuration.

Figure 15 gives the map of the strain component ε_{11} along the tensile axis for the pancake grains (Figures 15(a) and (b)) and for the recrystallized grains (Figure 15(c)). At the interface (Figure 15(a)), strain is homogeneous in both cases within all zinc grains and almost equal to the macroscopic strain $E_{11} = 1$ pct. This confirms that the substrate dictates its deformation to the coating, at least at the interface. In constrast, the strain maps are very different at the free surface (Figures 15(b) and (c)). For the NSK coating, strain localizes slightly at the grain boundaries but remains rather homogeneous within the zinc grains (Figure 15(b)). For the recrystallized coating with thick grains, strain localization is much stronger and large deformation bands form, linking some grains together (Figure 15(c)). This means that the ratio $d/h = 3$ is small enough for the strain incompatibility between neighboring grains to influence the whole deformation of the grains. In particular, this generates a strong strain gradient from the interface to the free surface, contrary to the case of pancake grains.

This strain gradient predicted for the recrystallized coating can also be illustrated by the activity of slip systems. Figure 16 displays the activity of basal slip systems and pyramidal π_2 slip systems at the interface and at the free surface. The maps show the von Mises equivalent plastic strain computed separately for each system family (it means that, for the computation of these variables, the sum in Eq. [1] is taken over the slip systems of one chosen family only). At the interface, basal slip is slightly more important than pyramidal π_2 slip. Maxima of slip activity are located near grain boundaries. This is due to plastic-strain incompatibility between the grains, but also to the strong elastic anisotropy of zinc, at least at the beginning of plastic flow. While the pyramidal π_2 activity remains weak at the free surface, basal slip invades several grains with, however, a strong gradient from grain to grain. At the free surface, some grains are strongly plastically deformed, whereas other grains deform mainly elastically. The significant activation of basal slip at the free surface is in accordance with the experimental observations for the recrystallized coating.

V. CONCLUSIONS

1. The deformation of zinc coatings on hot-dip galvanized steel sheets proceeds through the activation of many slip systems belonging to several slip-system families. Basal slip is not the main deformation mechanism, except in the recrystallized coating. Pyramidal π_2 slip has been shown to be a major deformation mode in the NSK and SK coat-

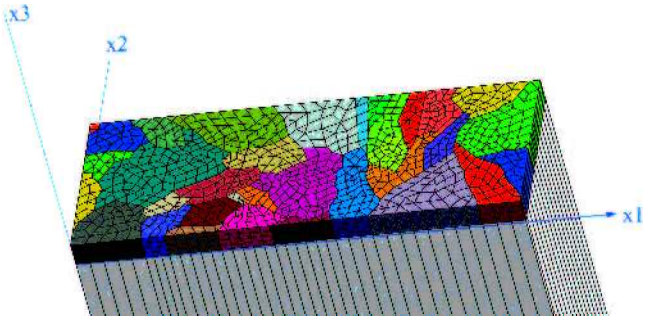

Fig. 14—Multicrystalline finite-element mesh for 34 small grains of a recrystallized coating (ratio $d/h \simeq 3$).

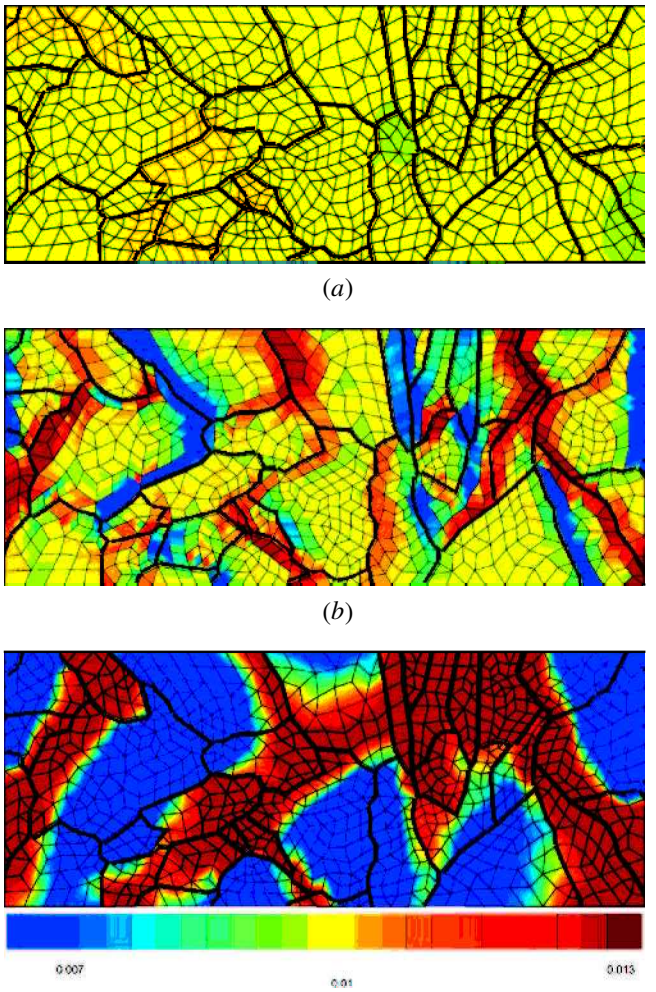

(*a*)

(*b*)

(*c*)

Fig. 15—Tensile strain map in the coating microstructure of Fig. 14 for two different grain sizes: (*a*) at the interface (identical map for both grain sizes), (*b*) at the free surface for pancake-like grains (NSK coating), and (*c*) at the free surface for small grains (recrystallized coating). In this latter case, the strain gradient from interface to free surface is much more pronounced. The tensile direction is the horizontal one. The same color scale is used for the three maps. The superpimposed thick lines represent the grain boundaries.

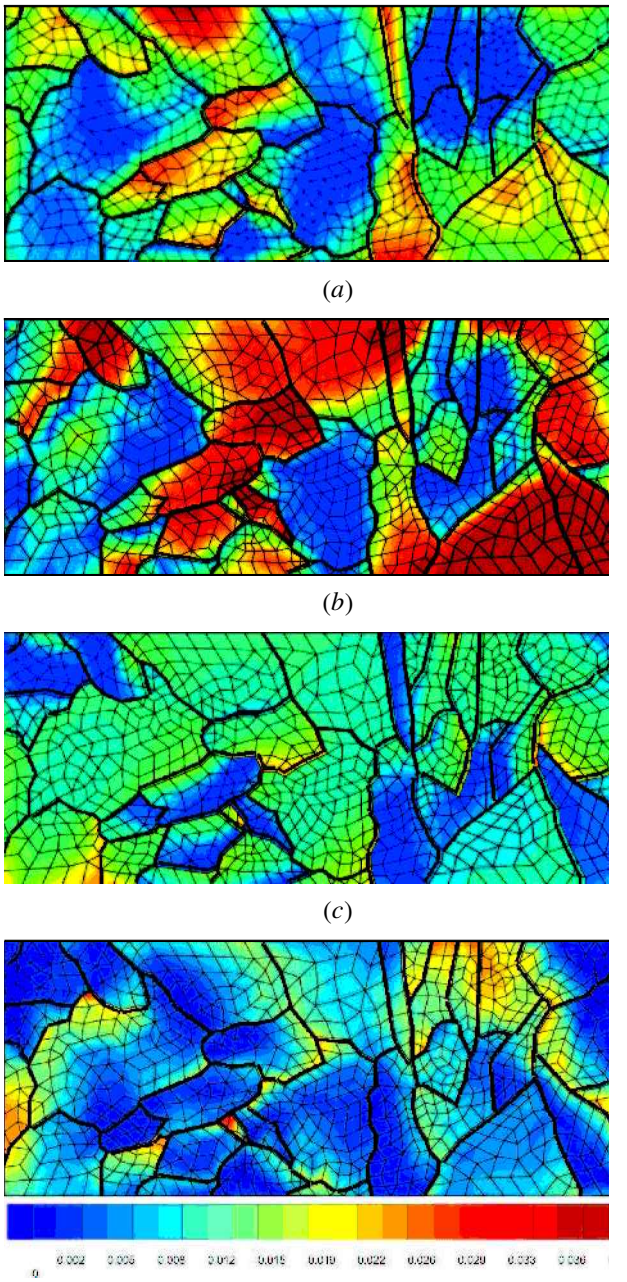

(*a*)

(*b*)

(*c*)

(*d*)

Fig. 16—Gradient of slip activity from the interface to the free surface for the recrystallized coating (*i.e.*, small grains): (*a*) equivalent plastic strain due to basal slip at the interface, (*b*) equivalent plastic strain due to basal slip at the free surface, (*c*) equivalent plastic strain due to pyramidal π_2 slip at the interface, and (*d*) equivalent plastic strain due to pyramidal π_2 slip at the free surface. The same color scale is used for all four maps. The superpimposed thick lines represent the grain boundaries.

ings. In contrast, the deformation of the reference bulk zinc alloy mainly involves basal slip, as expected from the literature on single and polycrystalline pure or alloyed zinc.

2. The recrystallized coating deforms in a way similar to the bulk material, at least at the free surface. This is true for the grains with an in-plane dimension of 30 to 50 μm. The case of larger grains still present in this microstructure is closer to the behavior of the NSK and SK coatings.
3. The previous conclusions are valid for uniaxial and biaxial overall loading conditions. When the biaxiality increases from tensile to expansion tests, the main difference is the increase of the number of deformation twins for all

investigated coatings, associated with a reduced activity of basal slip.

4. Twinning is a very important deformation mode in the NSK and SK coatings. Twin networks have been shown to nucleate and propagate in the pancake grains for all investigated loading conditions. In contrast, twinning does not occur in the bulk material and only occurs under biaxial loading conditions in the recrystallized coating.
5. A simple relaxed-constraint Taylor-like model has been used to model the substrate effect, *i.e.*, the constraining effect of the substrate that dictates its overall deformation to the individual grains of the NSK and SK coatings. This results in a strongly biaxial stress state in each grain, even for tensile global loading conditions. This complex stress state triggers the activation of many slip systems. The predictions of the model are consistent with the observations.
6. The ratio *d*/*h* between the in-plane grain size and the coating thickness is the most important parameter to explain the different responses of the investigated coatings. Fully three-dimensional finite-element computations of the substrate with a coating containing a finite number of grains prove that the simple Taylor model applies only when the ration *d*/*h* is large, *i.e.*, for pancake grains. In contrast, when *d*/*h* becomes of the order of 3 to 5, a significant gradient of stress and strain develops within the thickness of the coating. Basal slip is shown to dominate at the free surface under these conditions, as observed experimentally. We insist on the fact that the advocated effect is not strictly an absolute grain-size effect, but a morphological effect of the aspect ratio *d*/*h*.

More quantitative comparisons between the model and the experimental observations are necessary. In particular, the analysis was restricted to the comparison of the relative activation of slip systems, relying on the observation of slip traces at the free surface. The presence and the number of slip lines is not necessarily easily correlated to the corresponding strain amounts. However, the simulations involving material parameters identified from the literature and our tests do not reveal any bias associated with the observation technique. Quantitative comparisons require the use of local strain-or stress-measurement methods such as grids or image correlation. This has not been undertaken in this work.

Several additional features of the deformation of ductile coatings can be studied using the powerful multicrystalline simulation approach used in the present study. For example, the roughness of the interface substrate/coating, clearly visible in Figure 3, is not taken into account. Some effects of a periodic roughness have been numerically investigated in Reference 29. Conversely, the roughness induced by plasticity in the zinc grains can be predicted and is the subject of future work, because of its major importance in practice.[30]

In Part II of this article,[5] the constitutive model is combined with a cleavage criterion to predict damage initiation.

APPENDIX

Hardening-interaction matrix and material parameters for a single-crystal model

The hardening law, *i.e.*, the evolution of CRSS with plastic slip, used in the numerical simulation has the following form:

$$\tau_c^s = \tau_{0c}^s + \sum_{r=1}^{N} Q^s H_{rs}\left(1 - \exp\left(-b_r \gamma_{\text{cum}}^r\right)\right) \quad [A1]$$

where N is the total number of slip systems, including basal and nonbasal ones, and γ_{cum}^r is the cumulative plastic slip defined in the text. The parameter b^s denotes the saturation rate of hardening, and H_{rs} is the interaction matrix. It accounts for interaction between slip systems belonging to the same family, but also for interaction between slip systems of different slip-system families. An idealized form of the matrix is as follows:

$$\left(Q^s H_{rs}\right) = \begin{array}{c} \\ \text{basal} \\ \text{prism} \\ \pi_2 \\ \vdots \end{array} \begin{array}{c} \begin{array}{ccc} \text{basal} & \text{prism} & \pi_2 \end{array} \quad \cdots \\ \begin{pmatrix} \boldsymbol{Q}^b \begin{pmatrix} \boldsymbol{h}_1^b & \boldsymbol{h}_2^b & \cdots \\ \boldsymbol{h}_2^b & \boldsymbol{h}_1^b & \cdots \\ \boldsymbol{h}_2^b & \boldsymbol{h}_2^b & \cdots \end{pmatrix} & \boldsymbol{Q}^b h_p^b & \boldsymbol{Q}^b \boldsymbol{h}_{\pi_2}^b & \cdots \\ Q^p h_p^b & Q^p \begin{pmatrix} h_1^p & h_2^p & \cdots \\ h_2^p & h_1^p & \cdots \\ h_2^p & h_2^p & \cdots \end{pmatrix} & Q^p h_{\pi_2}^p & \cdots \\ \boldsymbol{Q}^{\pi_2} \boldsymbol{h}_{\pi_2}^b & \boldsymbol{Q}^{\pi_2} h_{\pi_2}^p & \boldsymbol{Q}^{\pi_2} \begin{pmatrix} \boldsymbol{h}_1^{\pi_2} & \boldsymbol{h}_2^{\pi_2} & \cdots \\ \boldsymbol{h}_2^{\pi_2} & \boldsymbol{h}_1^{\pi_2} & \cdots \\ \boldsymbol{h}_2^{\pi_2} & \boldsymbol{h}_2^{\pi_2} & \cdots \end{pmatrix} & \cdots \\ \vdots & \vdots & \vdots & \cdots \end{pmatrix} \end{array} \quad [A2]$$

The bold-faced italicized letters of the matrix of Eq. [A2] were identified from literature data. The diagonal terms of the submatrices are called self-hardening coefficients, whereas the out-of-diagonal terms correspond to latent hardening. The coefficient h_i^s is dimensionless and the parameter Q^s has the dimension of stress. Edwards and Washburn[31] worked on the latent hardening of a basal system in zinc, and the interpretation of their results leads to the following values: $Q^b \equiv 1$ MPa, $b_b \equiv 3$, $h_1^b \equiv 1$, and $h_2^b \equiv 2$. These values are consistent with the experimental results provided by Stofel and Wood[8] and

by Bosin *et al.*[32] Using, respectively, tension/torsion tests on single crystals and compression tests on bicrystals, the latter authors have studied the latent hardening for pyramidal π_2 slip and the interaction between basal and pyramidal π_2 slip. Latent hardening for a prismatic slip system was calculated by assuming that it has a similar behavior to basal and pyramidal π_2 slip systems, *i.e.*, $Q^p \simeq \tau_c^p$, $b_p \simeq 10$, and $h_1^p \equiv h_2^p \simeq 1$. No latent hardening was assigned to twinning.

The values of the remaining parameters in the model used in the simulations, especially the initial CRSS and hardening parameters, are deduced from the experimental results obtained in Reference 33 for a Zn + Al alloy. The reader is also referred to Reference 34 for the final identification of the parameters of a single-crystal zinc alloy using a homogenized polycrystal model and the experimental tensile, creep, and relaxation curves for the bulk zinc alloy. The hardening parameters found for pyramidal π_2 slip are $Q^{\pi 2} \equiv 15$ MPa, $b_{\pi 2} \equiv 30$, $h_1^{\pi_2} \equiv h_2^{\pi_2} \equiv 1$, and $h_{\pi_2}^b \equiv 2.8$.

The elastic anisotropy of a zinc single crystal is taken into account: the stiffness tensor **C** used for calculations is:

$$C_{11} = 165 \text{ GPa}, C_{22} = 165 \text{ GPa}, C_{33} = 61.8 \text{ GPa},$$

$$C_{12} = 31.1 \text{ GPa}, C_{23} = 50 \text{ GPa}, C_{13} = 50 \text{ GPa},$$

$$C_{44} = 19.8 \text{ GPa}, C_{55} = 19.8 \text{ GPa}, \text{ and } C_{66} = 33.5 \text{ GPa}$$

REFERENCES

1. S. Lazik, C. Esling, and J. Wegria: *Text. Microstr.*, 1996, vol. 23, pp. 131-47.
2. A.R. Marder: *Progr. Mater. Sci.*, 2000, vol. 45, pp. 191-271.
3. J. Lietzau, M.J. Philippe, C. Esling, J. Wegria, and M. Dubois: in *Zinc-Based Steel Coating Systems*, F.E. Goodwin, ed., TMS, Warrendale, PA, 1998, pp. 207-17.
4. C. Maeda, J. Shimomura, H. Fujisawa, and M. Konishi: *Scripta Metall.*, 1996, vol. 35, pp. 333-38.
5. R. Parisot, S. Forest, A. Pineau, F. Nguyen, X. Démonet, and J. M. Mataigne: *Metall. Mater. Trans. A*, 2004, vol. 35A, pp. 813-23.
6. P.G. Partridge: *Met. Rev.*, 1957, vol. 12, pp. 169-94.
7. R.L. Bell and R.W. Cahn: *Proc. R. Soc. A*, 1956, vol. 239, pp. 494-520.
8. E.J. Stofel and D.S. Wood: in *Fracture of Solids*, Metallurgical Society Conf., Aug. 21-24, 1963, vol. 20, pp. 521-39.
9. C. Tomé and U.F. Kocks. *Acta Mater.*, 1985, vol. 33, pp. 603-21.
10. R. Parisot, S. Forest, A.-F. Gourgues, A. Pineau, and D. Mareuse: *Comput. Mater. Sci.*, 2001, vol. 19, pp. 189-204.
11. Y. Leprêtre, J.-M. Mataigne, M. Guttmann, and J. Philibert: in *Zinc-Based Steel Coating Systems*, F.E., Goodwin ed., TMS, Warrendale, PA, 1998, pp. 95-106.
12. N.Y. Tang: in *Zinc-Based Steel Coating Systems*, F.E. Goodwin, ed., TMS, Warrendale, PA, 1998, pp. 3-12.
13. J. Strutzenberger and J. Faderl: *Metall. Mater. Trans. A*, 1998, vol. 29, pp. 631-46.
14. J.W. Christian: *The Theory of Transformation in Metals and Alloys*, Pergamon Press, Elmsford, NJ, 1965.
15. D.H. Rogers and W.T. Roberts: *Int. J. Mech. Sci.*, 1968, vol. 10, pp. 221-29.
16. A.-F. Gourgues: *Mater. Sci. Technol.*, 2002, vol. 18, pp. 119-33.
17. R. Parisot, S. Forest, A. Pineau, and X. Démonet: in *Advance in Mechanical Behaviour, Plasticity and Damage—Euromat 2000*, D. Miannay, P. Costa, D. François, and A. Pineau, ed., 2000, vol. 1, pp. 407-12.
18. K.M. Jassby and T.J. Vreeland: *Mater. Sci. Eng.*, 1977, vol. 27, pp. 1-9.
19. F.F. Lavrentev, O.P. Salita, and V.L. Vladimirova: *Phys. Status Solidi*, 1968, vol. 29, pp. 569-74.
20. J.J. Gilman: *Trans. TMS-AIME*, 1958, vol. 200, pp. 783-91.
21. J.J. Fundenberger, M.J. Philippe, F. Wagner, and C. Esling: *Acta Mater.*, 1997, vol. 45, pp. 4041-55.
22. D.E. Solas, C.N. Tomé, O. Engler, and H.R. Wenk: *Acta Mater.*, 2001, vol. 49, pp. 3791-3801.
23. U.F. Kocks and G.R. Canova: in *Deformation of Polycrystals*, Hansen *et al.*, eds., Ris∅ National Laboratory, Roskilde, Denmark, 1981, pp. 35-44.
24. P. Van Houtte: in *ICOTOM 6*, S. Nagashima, ed., The Iron and Steel Institute of Japan, Tokyo, 1981, pp. 428-37.
25. R.J. Asaro: *J. Appl. Mech.*, 1983, vol. 50, pp. 921-34.
26. H.J. Frost and M.F. Ashby: *Deformation-Mechanism Maps, The Plasticity and Creep of Metals and Ceramics*, Pergamon Press, Elmsford, NJ, 1982.
27. Z-set package. www.nwnumerics.com, www.mat.ensmp.fr., 2001.
28. R. Becker and S. Panchanadeeswaran: *Acta Metall. Mater.*, 1995, vol. 43, pp. 2701-19.
29. Rodolphe Parisot: Ph.D. Thesis, Ecole des Mines de Paris, Evry, 2001.
30. R. Becker: *Acta Mater.*, 1998, vol. 46, pp. 1385-1401.
31. E.H. Edwards and J. Washburn: *Trans. TMS-AIME*, 1954, vol. 200, pp. 1239-42.
32. M.E. Bosin, F.F. Lavrentev, and V.N. Nikiforenko: *Phys. Solid State*, 1996, vol. 38, pp. 1972-75.
33. K.H. Adams and T.J. Vreeland: *Trans. TMS-AIME*, 1968, vol. 242, pp. 132-39.
34. F. Barbe, R. Parisot, S. Forest, and G. Cailletaud: *J. Phys. IV*, 2001, vol. 11, pp. Pr5-277-Pr5-284.